Double-resonant Raman processes in germanium: Group theory and *ab initio* calculations

M. Mohr,* M. Machón, J. Maultzsch, and C. Thomsen
Institut für Festkörperphysik, Technische Universität Berlin, Hardenbergstr. 36, 10623 Berlin, Germany
(Received 9 September 2005; revised manuscript received 14 December 2005; published 31 January 2006)

We study the excitation-energy-dependent Raman peaks of germanium in terms of double-resonant scattering. In our analysis we combine group theory and *ab initio* calculations to select scattering processes and contrast them with the experimental data. A surface-driven *k*-selective mechanism explains not only the dependence of the peak shifts on surface orientation, but also their polarization dependence in a cubic system.

DOI: 10.1103/PhysRevB.73.035217 PACS number(s): 78.30.Am, 78.20.Bh, 02.20.−a

I. INTRODUCTION

Germanium is one of the elemental semiconductors and is widely used, e.g., in multilayer structures or quantum dots.[1,2] Its direct band gap of 0.89 eV makes it possible to study resonant Raman scattering effects with laser energies in the visible range.[3–5] Studying the shape of the Raman line near the $E_1+\Delta_1$ resonance, Gaisler *et al.*[6] discovered a low-energy phonon sideband near the optical phonons, which they attributed to a surface vibration. Recent calculations of surface vibrational modes of germanium nanocrystals of different sizes up to 7 Å show, however, that surface modes appear at energies far away from the optical phonons.[7] Mowbray *et al.*[8] found the side mode to shift with increasing laser energy and studied this behavior systematically for three different surfaces and several incident energies.

A shift of the Raman peaks with excitation energy was found as well for the acoustic phonons by Bansal *et al.*[9] Mowbray *et al.*,[8] and Bansal *et al.*[9] assigned these features to a double-resonant process occurring in the direction perpendicular to the Γ-L direction, near the critical gap $E_1+\Delta_1$. They found good agreement with the experiment. The polarization dependence in the optical range for measurements on the (110) surface and the appearance of three peaks in the acoustic range, however, remained somewhat puzzling. In particular it remained unclear why there is hardly no Raman signal in the optical range for the (100) surface whereas intense peaks are observed in the acoustic range. One might suspect differences in the selection rules for this surface compared to the other ones where the signal is observed.

In this paper we show that the excitation-energy dependence of both high- and low-energy modes can be explained in terms of double-resonant Raman scattering analogous to graphite and carbon nanotubes.[10–12] With the help of selection rules for the double-resonant process and *ab initio* calculations of band structure and phonon frequencies we examine which processes participate. Finally we present several methods to compare the theoretical model with the experimental observations, including a test of the electronic bands in the Brillouin zone.

In the next section we develop the theory of double-resonant Raman scattering and calculate the Raman cross section for a double-resonance model. We summarize the experimental data available in the literature. In Sec. III we present our *ab initio* electronic and phonon bands and develop selection rules for direct optical transitions and for scattering inside the Brillouin zone (BZ). In Sec. IV we introduce several allowed processes and show how to select the responsible double-resonant processes by applying several methods. In Sec. IV A a mathematical model for calculating the energy dependence of the Raman modes is developed. In Sec. IV B we compare the shifting Raman modes with the phonon dispersion. In Sec. IV C we show how the dispersion of the electronic bands can be obtained from double-resonant scattering.

II. DOUBLE-RESONANT RAMAN SCATTERING

We present first the experimental evidence from the literature for Raman modes which shift with excitation energy. Raman spectra measured on the (110) and (111) surfaces for different excitation energies are shown in Fig. 1(a). The small peak to the left of the zone-center phonon at 304 cm^{-1} shifts to lower energies with increasing incident energy. The shifts in the optical and acoustic range for several surfaces are summarized in Fig. 1(b). A dependence of the frequency shift on the scattering geometry is observed. Compare, for example, the data for the (110) and (111) surfaces in Fig. 1(b). For the (110) surface the peak positions for two different polarizations are shown and a difference in the shift rate is observed (9 and 14 cm^{-1}/eV for the two polarizations; see Table III). We have thus the curiosity that the Raman frequency of a peak appears to depend on polarization, an effect also seen in superlattices.[13]

To illustrate a double-resonant Raman process we show the scattering in an idealized electronic band scheme. In Fig. 2(a) an incoming photon with laser energy E_l resonantly excites an electron-hole pair ($i \rightarrow a$). The excited electron is scattered by phonons with arbitrary wave vector q. The scattering probability is especially high if the phonon scatters the electron from the real electronic state a into another real electronic state $b(a \rightarrow b)$ [Fig. 2(b)]. From there the electron is scattered back elastically ($b \rightarrow c$) to a virtual state c, where the electron-hole pair finally recombines ($c \rightarrow f$), emitting the photon energy $E_l - \hbar\omega_{ph}(q)$ (Stokes scattering). In Fig. 2(c) the same process is shown for a larger incident laser energy $E_l' > E_l$. A phonon with different wave vector q' and, assuming the phonon dispersion of Fig. 2(d), with smaller energy $\hbar\omega_{ph}(q')$ is selected by the double-resonant process. This leads to a downshift of the peak in the Raman spectra with increasing incident energy.

The matrix element $K_{2f,10}$ of a Raman process can be calculated with[14–16]

$$K_{2f,10} = \sum_{a,b,c} \frac{M_{fi}}{(E_l - E_{ai} - i\hbar\gamma)(E_l - \hbar\omega_{ph} - E_{bi} - i\hbar\gamma)(E_l - \hbar\omega_{ph} - E_{ci} - i\hbar\gamma)}, \quad (1)$$

where E_{ai} is the energy difference between the electronic state i and a [correspondingly for the other electronic states as denoted in Fig. 2(b)]. E_l and $E_l - \hbar\omega_{ph}$ are the energies of the incoming and outgoing photons, respectively. M_{fi} is the combined matrix element for the scattering over all intermediate states between i and f, and γ is the broadening parameter of the electronic transitions.

In double resonance two of the terms in the denominator of Eq. (1) give a large contribution. Identifying $E_{ai} = E(\vec{k}) - E_l$ and $E_{bi} = E(\vec{k}+\vec{q}) - E_l$ leads to the resonance condition

$$E_{c/v}(\vec{k}) \mp \hbar\omega_{ph}(\vec{q}) = E_{c/v}(\vec{k}+\vec{q}), \quad (2)$$

where the minus sign corresponds to a resonance in the incoming channel and the plus sign to a resonance in the outgoing channel. The index c/v indicates scattering in the conduction (CB) or valence band (VB), respectively. For parabolic electronic and phonon bands two phonons fulfill Eq. (2): one for scattering across the valley and one for scattering in the vicinity of the initial k value. The latter cancels due to destructive interference if a full integration over all intermediate states of the cross section $|K_{2f,10}|^2$ is performed.[17]

Such double-resonant processes were observed also in one-dimensional (carbon nanotubes) and two-dimensional (graphite) materials.[10–12,17] Martin and Falicov[16] pointed out that there are different types of resonant enhancements, depending on the shape and dimension of the involved band structures. To analyze if and what type of resonance is to be expected in a three-dimensional system, we calculated the cross section from Eq. (1) for linear bands. We extended the calculation by Maultzsch *et al.*[17] by performing a full integration in three dimensions. The contributions of all allowed processes were integrated, irrespective of whether they were resonant or not. The results are shown in Fig. 3 for an integration in one, two, and three dimensions. As in the extension from one to two dimensions, the main difference in three dimensions is the broader range of double-resonant phonon vectors. The positions of the maxima—i.e., the phonon wave vectors that contribute mostly to the double resonance—remain the same in all calculations. The results show that the dominant contribution comes from the scattering across the Γ point as in one dimension. An integration in one dimension is therefore sufficient to find the double-resonant phonon wave vectors with the strongest Raman signal.

III. CALCULATION

First we present *ab initio* calculations of the Ge band structure. Then we discuss the selection rules relevant to double-resonant Raman scattering and show which processes are allowed on which surface.

A. *Ab initio* calculation of electronic and vibrational bands

Ab initio calculations were performed with the SIESTA code[18,19] using the functional in the local density approximation of Perdew-Zunger[20] and Troullier-Martins[21] pseudopotentials. An equivalent energy cutoff of 40 Ry was used for the real-space grid integrations and a $(5\times5\times5)$ Monkhorst-Pack[22] mesh in reciprocal space. The valence electrons were described by a double-ζ basis set with cutoff radii of 6.42 and 8.88 bohrs for the s and p orbitals, respectively, plus an additional polarizing orbital. We obtain an equilibrium lattice constant of 5.63 Å after relaxation and taking into account the zero-point renormalization, as described in Ref. 23, in good agreement with the experimental value of 5.66 Å.

The calculated band structure of germanium is shown in Fig. 4; the conduction bands were shifted up rigidly by 0.38 eV to match the experimental gap. The energy origin lies at the valence band maximum. For comparison we also show the bands of a nonorthogonal tight-binding calculation on a sp^3d^5 basis.[24] Both calculations are without spin-orbit interaction. The inset shows our band structure compared to a recent 30-band $\mathbf{k}\cdot\mathbf{p}$ method with spin-orbit interaction, showing that there are only little differences.[25] In Fig. 5 we show a close-up of the bands centered at $L/4$.

The phonon dispersion was obtained from the dynamical matrix. The force constant matrix was calculated using a finite-difference approach for the second derivative of the total energy.[26] The supercell contained 27 unit cells—i.e., 54 atoms—and the energy cutoff was increased to 60 Ry. The frequencies we obtained were multiplied by 1.015 to match the experimental frequencies of the optical phonon, $\omega_{\mathrm{opt}} = 304\ \mathrm{cm}^{-1}$. The calculated *ab initio* phonon dispersion (Fig. 6) is in excellent agreement with experimental data and will serve for further analysis of the double resonant scattering process.[27]

B. Selection rules

The crystal structure of germanium is the diamond lattice. The space group in Schönfliess notation is O_h^7 (international notation $Fd3m$) with the factor group O_h. The space group O_h^7 is nonsymmorphic, but since we consider only points inside the Brillouin zone and not at the zone boundary, no special considerations are required. Double-resonant Raman scattering is a fourth-order process; therefore, the square root intensity is

$$\sqrt{I} \propto |\langle f|H_{eR}|c\rangle\langle c|H_{eD}|b\rangle\langle b|H_{ep}|a\rangle\langle a|H_{eR}|i\rangle|. \quad (3)$$

H_{eR} denotes the electron-radiation interaction Hamiltonian, H_{ep} the electron-phonon interaction, and H_{eD} the electron-defect interaction Hamiltonian. In the case of graphite and nanotubes, k conservation is provided by defects. In the ex-

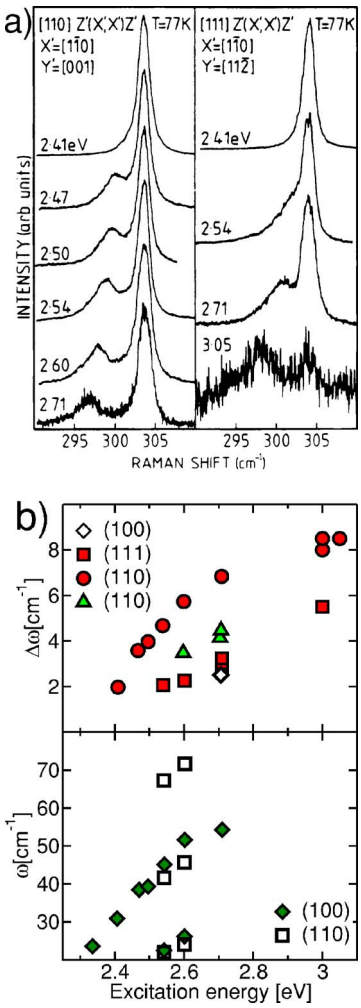

FIG. 1. (Color online) (a) Raman spectra of the (110) and (111) surfaces of germanium for various laser lines (from Ref. 8). (b) Shift of the energy-dependent Raman modes as a function of excitation energy. Upper plot: optical range ($\Delta\omega$ denotes the difference between the optical Γ-point phonon and the shifting mode). Circles denote measurements on the (110) surface with excitation light polarized parallel to the $[\bar{1}10]$ direction. Triangles: (110) surface and [001] polarization. Solid squares: (111) surface. Diamonds: (100) surface. Lower plot: acoustic shifting modes (ω in absolute wave numbers). Diamonds: (100) surface. Open squares: (110) surface (optical modes taken from Ref. 8, acoustic modes taken from Ref. 9).

periments discussed here, high-purity samples of Ge were used and defects cannot provide k conservation. Instead the surface provides the necessary quasimomentum. Since it is not clear what type of symmetry is expected for M_{eD}, we make no assumptions about this matrix element. We consider the selection rules for each matrix element in Eq. (3) individually and therefore obtain selection rules that are less restrictive than may be observed in experiment.

1. Selection rules for optical transitions

Calculating direct products with the dipole representation $\Gamma^{(D)}$ subduced in the subgroup of the corresponding k point

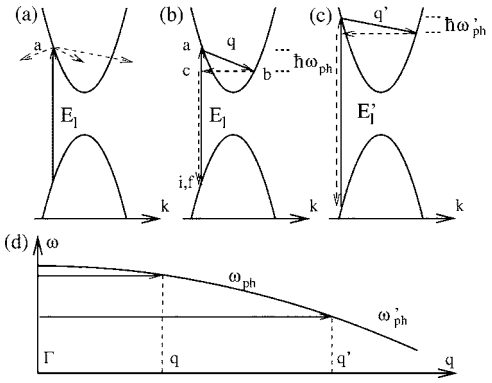

FIG. 2. Double-resonant Raman scattering for symmetric parabolic bands with a band gap. (a) Resonant excitation of an electron-hole pair followed by nonresonant scattering of the electron. (b) Double-resonant Raman scattering process: an electron is excited by a photon of energy E_l and scattered by a phonon of frequency ω_{ph} and momentum q. It is scattered back elastically by a defect and finally recombines. (c) For a different incoming photon energy E_l' the double-resonance condition selects a different phonon (ω_{ph}', q'). (d) Idealized vibrational dispersion curve showing the two phonons with momentum q and q'.

leads to the results in Table I.[28] In cubic crystals there are in principle no polarization-dependent selection rules for direct optical dipole transitions. This does not hold if some of the equivalent k points of a star in the BZ are preferred due to a k-selective mechanism, like surface scattering. The effect of the surface implies selection rules similar to uniaxial stress.[29] Consider, for example, an $x'(z,z)\bar{x}'$ setup on a (110) surface: an electron is excited to one of the six equivalent Δ axes. Then it is scattered by a Σ phonon to an equivalent Δ axis [Δ_t; see Fig. 7(b)]. Only electrons scattered back to the initial Δ axis by, e.g., a defect can recombine. A local defect (like a vacancy or a substitutional defect) is assumed to scatter in all directions, leading to a situation comparable to second-order Raman scattering.[30] Contrary to that, a surface transfers momentum only in the direction of the surface normal. Thus only those electrons scattered by phonons from Σ directions perpendicular to the surface contribute to the Raman cross section. This means for the (110) surface that only electrons on the Δ axes $[\bar{1}00]$ and $[0\bar{1}0]$ contribute to the double-resonant process.

Now for a $\Delta_{2'} \leftrightarrow \Delta_{2'}$ optical transition a polarization component parallel to one particular Δ axis is required (see Table

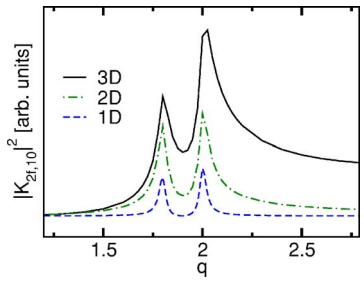

FIG. 3. (Color online) Raman cross section $|K_{2f,10}|^2$ as a function of the phonon wave vector for linear bands in one (blue, dashed line), two (green, dashed dotted line), and three (black, solid line) dimensions.

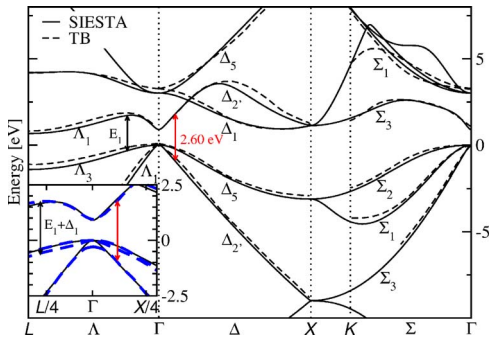

FIG. 4. (Color online) Band structure of germanium. Solid lines are our *ab initio* calculations. The dashed lines show a recent tight-binding calculation, also neglecting the spin-orbit interaction (Ref. 24) Band symmetries are given in single-group notation. Inset: close-up around the valence band maximum. The dashed lines show a 30-band $\mathbf{k}\cdot\mathbf{p}$ calculation including spin-orbit interaction which causes a maximal splitting in the L direction of Δ_1=0.2 eV (Ref. 25).

I); thus, only electrons on the $[00\xi]$ or $[00\bar{\xi}]$ axis are excited. But we have seen above that only Δ electrons from the $[\bar{1}00]$ or $[0\bar{1}0]$ axis can be scattered elastically by the (110) surface. Thus electrons are excited and scattered but the elastic process for recombination is missing, and this process does not contribute to the double-resonant cross section. In conclusion, in an $x'(z,z)\bar{x}'$ experiment for a (110) surface, the

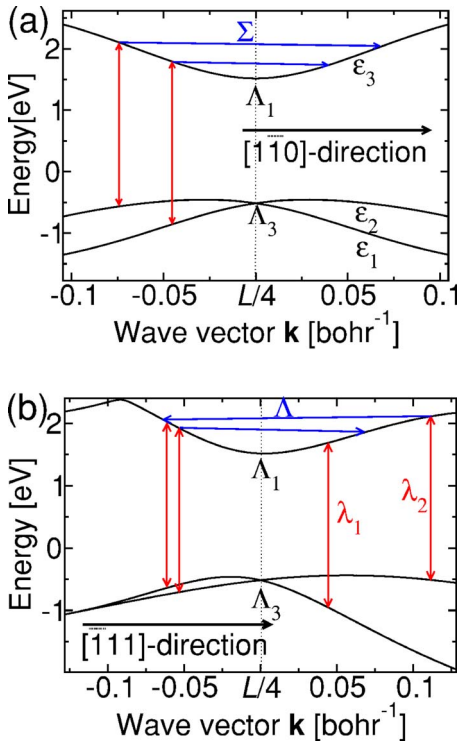

FIG. 5. (Color online) Two processes $\perp E_1$ illustrated in the electronic band structure. Vertical arrows indicate real transitions with an energy of 2.60 eV. (a) Electronic bands centered at $L/4$ in direction $[1\bar{1}0]$. Symbols ε_i $(i=1,2,3)$ are our notation. (b) Like in (a) but in direction $[\bar{1}11]$. Symbols $\lambda_{1,2}$ are our notation.

TABLE I. Selection rules for electronic dipole transitions. At each particular k point the main rotational axis defines the $\tilde{z}$ direction; e.g., for a Λ transition taking place at $[\bar{\zeta},\zeta,\zeta]\pi/a$, $\tilde{z}$ is along $[\bar{1}11]$.

Transition	Allowed polarizations
$\Lambda_1 \leftrightarrow \Lambda_1$	$\tilde{z}$
$\Lambda_1 \leftrightarrow \Lambda_3$	$\tilde{x}\tilde{y}$ plane
$\Delta_{2'} \leftrightarrow \Delta_1$	Forbidden
$\Delta_5 \leftrightarrow \Delta_{2'}$	$\tilde{x}\tilde{y}$ plane
$\Delta_5 \leftrightarrow \Delta_1$	$\tilde{x}\tilde{y}$ plane
$\Delta_{2'} \leftrightarrow \Delta_{2'}$	$\tilde{z}$
$\Sigma_m \leftrightarrow \Sigma_m$ $(m=1-4)$	$\tilde{z}$
$\Sigma_1 \leftrightarrow \Sigma_2$	Forbidden
$\Sigma_1 \leftrightarrow \Sigma_3$	$\tilde{y}$
$\Sigma_2 \leftrightarrow \Sigma_3$	$\tilde{x}$

double resonance with a $\Delta_{2'} \leftrightarrow \Delta_{2'}$ transition does not contribute to the cross section. For four of the equivalent Δ axes the transition is forbidden and for the remaining two axes the elastic scattering needed for k conservation cannot be provided. In contrast, a $\Delta_5 \leftrightarrow \Delta_{2'}$ transition does contribute. For such a transition, electrons that fulfill the resonance condition have a larger wave vector k as for a $\Delta_{2'} \leftrightarrow \Delta_{2'}$ transition and with that phonons with larger wave vector q and smaller energy are involved in the double-resonant process. On the basis of these arguments the polarization dependence for the (110) surface can be explained.

2. *Connecting different points in the BZ*

The symmetry-allowed processes in which an electron is scattered by a phonon were obtained as follows. The initial eigenfunction $\Psi_a(\mathbf{r})$, the final eigenfunction $\Psi_b(\mathbf{r})$, and the perturbation $V'(\mathbf{r})$ transform as the irreducible representations Γ^{kp}, $\Gamma^{k''p''}$, and $\Gamma^{k'p'}$, respectively. k denotes the wave vector and p specifies the irreducible representation of the group of k $[\mathcal{G}_0(k)]$. The symmetrized product of the representations of states a and b must contain the representation $\mathbf{\Gamma^{k'p'}}$,

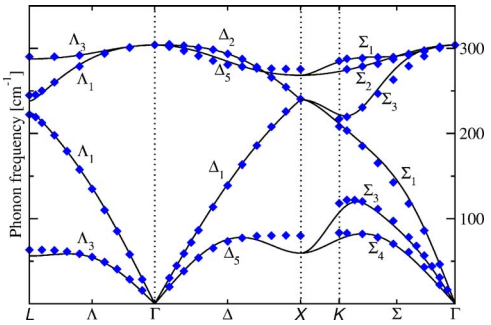

FIG. 6. (Color online) Phonon dispersion of germanium. The solid lines denote our calculations; the diamonds denote data from inelastic neutron scattering (Ref. 27).

TABLE II. Selection rules for electron scattered by phonons. Left column: symmetry of the electronic bands. Right column: allowed phonons. See text for an explanation of the symbols.

Symmetry of Ψ_a, Ψ_b	Allowed phonons
Across Γ	
$\Lambda_i \leftrightarrow \Lambda_i$ $(i=1,2)$	Λ_1 (LO,LA)
$\Delta_i \leftrightarrow \Delta_i$ $(i=1,2)$	Δ_1 (LA)
$\Sigma_i \leftrightarrow \Sigma_i$ $(i=1-4)$	Σ_1 (TO,LA)
$\Delta_5 \leftrightarrow \Delta_5$	Δ_1 (LA), Δ_2 (—), $\Delta_{2'}$ (LO)
$\Lambda_3 \leftrightarrow \Lambda_3$	Λ_1 (LO,LA), Λ_3 (TO,TA)
Not across Γ	
$\perp E_1$	Any Σ
$\Delta_1 \leftrightarrow \Delta_{1t}, \Delta_2 \leftrightarrow \Delta_{2t}$	Σ_1 (TO,LA)
$\Delta_5 \leftrightarrow \Delta_{5t}$	Σ_1 (TO,LA), Σ_2 (TO), Σ_3 (LO,TA)
$\Lambda_1 \leftrightarrow \Lambda_{1t}$	Δ_1 (LA), $\Delta_{2'}$ (LO)
	Σ_1 (TO,LA)
$\Lambda_3 \leftrightarrow \Lambda_{3t}$	Any Δ
	Σ_1, Σ_2, Σ_4

$$(\Gamma^{\mathbf{kp}} \otimes \Gamma^{\mathbf{k''p''}})_{\mathrm{sym}} \supset \Gamma^{\mathbf{k'p'}}, \tag{4}$$

for a nonvanishing matrix element. The allowed phonons shown in Table II are obtained by evaluating the symmetrized product of the involved bands. The index t denotes different branches of a given star. For some entries in Table II we used the subgroup methods described by Lax and Hopfield.[31,32] Others were taken from Ref. 33.

C. Double-resonant processes in Ge

In Refs. 8 and 9 the process shown schematically in Fig. 8(a) was proposed. We denote this process "$\perp E_1$." The following arguments show that this cannot be the only relevant process. Without further assumptions (like two-phonon scattering) this process cannot explain the appearance of three peaks in the acoustic range of a (110) surface. Zhang *et al.*[34] have found a small but systematic difference of the optical phonon linewidth in Ge samples for different orientations and for several excitation energies. The difference becomes

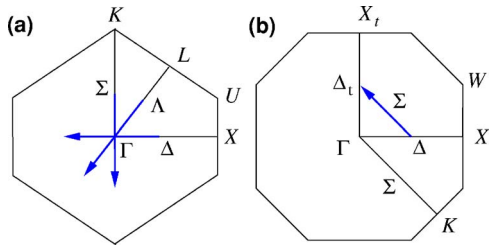

FIG. 7. (Color online) (a) Processes across Γ are shown on the plane of the Brillouin zone spanned by the directions Δ and Λ. (b) $\Delta\Delta_t$ process shown on the plane of the Brillouin zone spanned by the directions Δ and Σ.

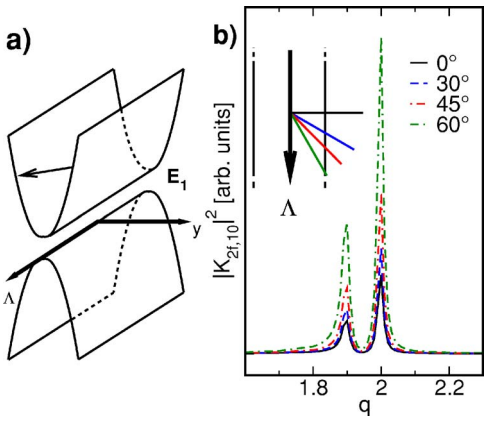

FIG. 8. (Color online) (a) Process $\perp E_1$ illustrated in a band model for the electronic bands along Λ. (b) Raman cross section $|K_{2f,10}|^2$ as a function of the phonon wave vector for the parabolic valleylike bands shown in (a), calculated with the direction of **k** fixed. The angle quoted is between the directions of **k** and y.

smaller but remains present for laser energies below the critical $E_1+\Delta_1$ gap.

A real transition and with it a double resonance can also occur in the vicinity of the Γ point.[35] We therefore consider also scattering of the electron "across Γ" between bands of the same symmetry [see Fig. 7(a)]. Between nondegenerate bands this is only possible with a fully symmetric phonon. For the (110) surface we also consider scattering from one Δ axis onto another Δ axis with a Σ phonon [referred to as $\Delta\Delta_t$ scattering and shown in Fig. 7(b)].

Summarizing, based on the experiments and the selection rules presented in the preceeding sections, we consider the following processes: "$\perp E_1$," "across Γ," and "$\Delta\Delta_t$." These processes will be tested by several means in the next section.

The Raman cross-section calculation presented in Sec. II is a good approximation to the processes across Γ. We now want to perform an equivalent calculation for the process "$\perp E_1$." In Fig. 8(a) we show the model used for the calculation of the double-resonant cross section perpendicular to Λ. We performed a full integration in two dimensions with the direction of k fixed. The cross section as a function of the absolute value of the phonon wave vector q is shown in Fig. 8(b) for four different directions. The angle quoted is between the directions of k and y. Independent of the direction of the electron wave vector k the double-resonant process enhances phonons with the same absolute value of wave vector q. The corresponding bands for the $\Delta\Delta_t$ have a similar form as shown in Fig. 8(a). In this case the valley flattens approaching the Γ point. The range of k points in which an optical absorption of energy E_l can take place is, however, small compared to the length of the Δ axis. Therefore we can approximate this scattering process with the model we just discussed.

IV. COMPARISON WITH EXPERIMENTAL DATA

A. Calculation of the slope $\partial\omega/\partial E_l$

Following the model of Ref. 8 we derived a quantity that can be compared directly with the experiment: the observed

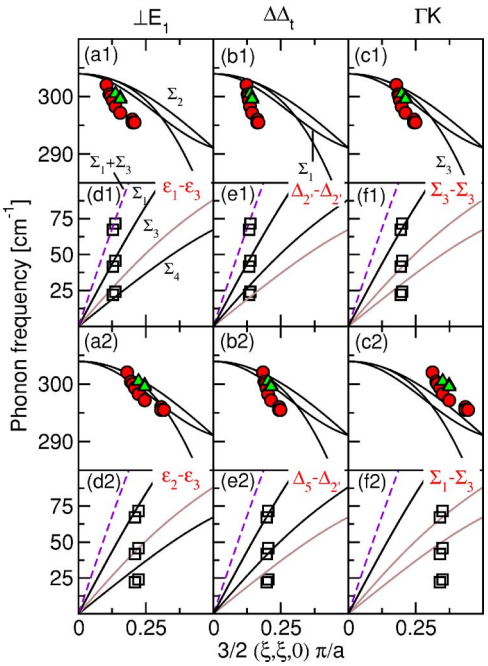

FIG. 9. (Color online) Mapping of the Raman modes measured on a (110) surface onto the phonon dispersion. For the modes the same symbols as in Fig. 1(b) were used. Lines denote our calculated phonon dispersion. Underlying processes are written above the columns. The first and third rows [panels (a)–(c)] show optical modes whereas the second and fourth rows [panels (d)–(f)] show acoustic modes. The panels numbered with 1 and 2 correspond to different underlying optical transitions. The corresponding transitions (denoted in red) can be seen in Figs. 4 and 5(a). The same processes were assumed for the peaks in the optical and acoustic ranges of each of the six pairs. Grey lines (brown online) in the acoustic spectrum denote phonons that are forbidden for the actual process.

shift rate of a Raman peak with excitation energy $\partial\omega/\partial E_l$. From the double-resonance condition, Eq. (2), we find

$$\frac{\partial\omega}{\partial E_l} = \frac{\partial\omega}{\partial q}\frac{\partial q}{\partial E_l} \tag{5}$$

for one-dimensional bands. Consider parabolic bands—i.e., $E_c(k)=e_{2c}k^2+e_0$ and $E_v(k)=-e_{2v}k^2$ for the electrons and $\omega(q)=Aq^2+\omega_0$ for the phonons. Solving Eq. (2) for k gives

$$k = -\frac{e_{2c}q+\hbar Aq+\hbar\omega_0}{2e_{2c}q}, \tag{6}$$

determining the wave vector k of the scattered electron for a phonon momentum q in a double-resonant process. Inserting k into the resonance energy $E_l(k)=E_c(k)-E_v(k)$ gives E_l as a function of the phonon momentum q and the derivative of the inverse function $q'(E)=\partial q/\partial E_l$. Finally, we obtain

$$\frac{\partial\omega}{\partial E_l} = -\frac{4Ae_{2c}^2q^4}{(e_{2c}+e_{2v})[e_{2c}^2q^4+2\hbar Ae_{2c}q^4+\hbar^2(A^2q^4-\omega_0^2)]}$$
$$\cong -\frac{4Ae_{2c}^2q^4}{(e_{2c}+e_{2v})e_{2c}^2q^4} = -\frac{4A}{(e_{2c}+e_{2v})}. \tag{7}$$

The two terms $2\hbar Ae_{2c}q^4$ and $\hbar^2(A^2q^4-\omega_0^2)$ are several orders

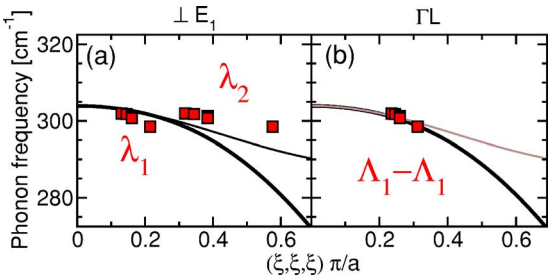

FIG. 10. (Color online) Mapping of the Raman peaks measured on a (111) surface onto the phonon dispersion as described in the text. Same symbols as in Fig. 1(b) were used. Underlying processes are (a) $\perp E_1$ and (b) ΓL. $\lambda_{1,2}$ denote the transitions in Fig. 5(b).

of magnitude smaller than $e_{2c}^2q^4$ and can therefore be neglected. Since Eq. (7) is independent of e_0 and ω_0, the fit of the bands does not have to represent well the band gap or the Γ-point phonon frequency, respectively. We therefore approximate the bands in the region of the optical transition of the laser light. This leads to a more accurate description of the double-resonant (DR) process even though the parabolic band approximation is still not optimal. We calculated a similar expression for bands approximated by an even fourth-order polynomial, $E_{c/v}(k)=e_{4c/v}k^4+e_{2c/v}k^2+e_{0c/v}$, which represents a fairly good approximation for the bands in the vicinity of the Γ point and the valley perpendicular to the ΓL direction at E_1.

In Table III the values of $\partial\omega/\partial E_l$ for parabolic and for fourth-order bands are given. Apart from the process denoted as ΓK ($\Sigma_2\leftrightarrow\Sigma_3$), all processes yield values of $\partial\omega/\partial E_l$ in reasonable agreement with the experimental observations. This supports the idea of several processes being responsible for the behavior of the Raman modes.

In the following we show further more sensitive means of comparing our theoretical model with the experimental data.

B. Phonon dispersion from double-resonant Raman scattering

The change in phonon frequency with excitation energy is the characteristic feature of a double resonance. The shift of the double-resonant Raman mode can be used to find the phonon dispersion. This approach was suggested by Thomsen and Reich[10] and applied to graphite by Saito *et al.*[36] We proceed as follows: at a given excitation energy the electron wave vector k_e is obtained from the electronic band structure. The frequency of the observed Raman peak is then plotted at the wave vector selected by the double-resonance condition, and the phonon dispersion is obtained.[12,37]

We mapped the (110)-surface measurements using the processes proposed in Sec. III C. The results are summarized in Fig. 9. The circles and triangles in the optical range denote different experimental geometries, whereas the squares in the acoustic range plotted on top of each other stem from the same spectrum.

Let us consider first the optical modes. For the $\Delta\Delta_t$ process we find a good agreement of the mapped data to the calculated phonon dispersions. This process can explain the

TABLE III. Comparison of the mode dispersion $\partial\omega/\partial E_l$ to experiment for parabolic and fourth-order fits to the calculated dispersion for the optical DR modes. Left column: scattering process. In parentheses are the underlying optical transitions. The numerical values are all in cm^{-1}/eV. Beside them, the symmetries of the phonons used in the calculation are indicated in brackets. The slope in the fourth-order model depends on q. We give therefore a range corresponding to a laser energy between 2.4 and 3 eV.

Surface	(110)		(111)
polarization	$\parallel[\bar{1}10]$	$\parallel[001]$	—
Experiment[a]	14	9	6
Calc. parabolic			
ΓL			5.2 (Λ_1)
$\perp E_1$ ($\varepsilon_2 \leftrightarrow \varepsilon_3$)[b]	8.1 (Σ_1)		
$\perp E_1$ ($\varepsilon_1 \leftrightarrow \varepsilon_3$)[b]		3.8(Σ_1)	
ΓK ($\Sigma_3 \leftrightarrow \Sigma_3$)	3.8(Σ_1)	3.8(Σ_1)	
ΓK ($\Sigma_1 \leftrightarrow \Sigma_3$)	17(Σ_1)	17(Σ_1)	
ΓK ($\Sigma_2 \leftrightarrow \Sigma_3$)	75(Σ_1)	75(Σ_1)	
$\Delta\Delta_t$ ($\Delta_5 \leftrightarrow \Delta_{2'}$)	3.7 (Σ_1)		
$\Delta\Delta_t$ ($\Delta_{2'} \leftrightarrow \Delta_{2'}$)		2.8 (Σ_1)	
Calc. fourth-order			
ΓL ($\Lambda_1 \leftrightarrow \Lambda_1$)			4.3–6.8
$\perp E_1$ ($\varepsilon_2 \leftrightarrow \varepsilon_3$)[b]	6.5–10.5 (Σ_1)		
$\perp E_1$ ($\varepsilon_1 \leftrightarrow \varepsilon_3$)[b]		3–5(Σ_1)	

[a]From Ref. 8.

[b]This transition was tentatively assumed. Corresponding bands in Fig. 5(a).

observed polarization dependence as discussed in Sec. III B 1. The surface provides a *k*-selective mechanism that selects particular axes of a star, leading to polarization-dependent optical transitions. The triangles and circles in Fig. 9 represent the modes corresponding to the two polarizations used in the experiment. The agreement of the mapping with the calculated phonon dispersion supports this explanation. In the acoustic range, the peaks at around 24 cm^{-1} and 48 cm^{-1} match well the calculated dispersions [panel (e1)]. The same applies in (e2) for the peaks at 48 cm^{-1} and 70 cm^{-1}. But following the same arguments as in the optical range only one transition is allowed for each experimental geometry so that an additional process is needed to explain three peaks in the acoustic range.

For the $\perp E_1$ process the mapping matches the vibrational dispersion as well. The mapping shown in Figs. 9(a1) and 9(a2) leads to a good agreement. In the acoustic range we find in (d1) a good agreement for the peaks at 24 cm^{-1} and 48 cm^{-1} and in (d2) for the peaks at 24 cm^{-1} and 70 cm^{-1}. Therefore, assuming a similar polarization dependence as for the $\Delta\Delta_t$ process we can explain the experimental observations. For the optical range in the ΓK process we find a good agreement for the triangles in (c1) and the circles in (c2). In the acoustic range only the peak at 70 cm^{-1} in (f1) fits our phonon dispersion.

A scattering by two phonons $\Sigma_1+\Sigma_3$ (dashed line) is supported by some processes [Figs. 9(d1) and 9(e1)]. But since wave vector conservation can always be fulfilled with two phonons of opposite direction, these modes should be independent of the surface and should be seen for other surfaces as well, which up to now has not been reported.

Note that for measurements on the (110) surface with excitation light parallel to [001] (triangles) Raman scattering is forbidden by the usual Raman tensor. This indicates that the elastic scattering process changes the symmetry of the intermediate state.

In Fig. 10 we show the mapping of the optical modes measured on the (111) surface. No data in the acoustic range are available for this surface. The relevant optical transitions for the $\perp E_1$ process [Fig. 10(a)] are shown in Fig. 5(b). We only use the transitions leading to the smallest and biggest wave vector q (λ_1 and λ_2, respectively). The points in Fig. 10(b) correspond to a scattering across Γ and to an underlying $\Lambda_1 \leftrightarrow \Lambda_1$ transition. They match well the fully symmetric phonon Λ_1 (bold line), which is the only symmetry-allowed phonon for this process.

As we have seen, the discussion for the optical modes is more difficult since the optical phonons are much less dispersive. The fully symmetric Σ_1 phonon, for example, has a bandwidth of 20 cm^{-1}. Further measurements especially in the acoustic range are desirable to verify our results. Additionally we expect a polarization dependence for the acoustic modes on a (110) surface. More work on the polarization dependence of optical transitions for general points in the Brillouin zone, as those in Fig. 5, could help to interpret the experimental results.

C. Electron mapping

In the last section we showed how to compare the experimental results to the theoretical predictions with the help of the calculated electronic and phonon bands. One main disadvantage is that the wave vector k_e of the resonant transition is extracted from the electronic bands. Our *ab initio* calculations were done using density functional theory, known to predict well the electronic VB and the phonon dispersion curves, but to underestimate the energies of the CB. Therefore the absolute value of k_e is overestimated, especially for weakly dispersive electronic bands.

Here we show how we can map, *vice versa*, the experimental data onto the *electronic* band structure of germanium using our calculated phonon dispersion. The observed Raman peak corresponds to a phonon with wave vector $q \neq 0$. Looking for the measured frequency in the calculated phonon dispersion curves we obtain the value q. To choose the phonon the selection rules in Table II are used. The excitation energy E_l in the experiment is then added to the energy of the corresponding valence band at the k vector selected by the double-resonance condition.

The resulting energies for the acoustic and optical phonon peaks are plotted in Fig. 11. The calculated energies for the Δ_5 and $\Delta_{2'}$ bands (solid lines) tend to be too high compared with the experimental data (blue squares and open circles). The mapped double-resonant data points mimic well the shape of the conduction bands and are within same experimental errors as the inverse photoemission spectra. The mapping described here can be used to obtain electronic energies at wave vectors $\mathbf{k} \neq 0$ if the double-resonant process is known. Additionally double-resonant processes from acoustic and optical phonons can be directly compared with this mapping.

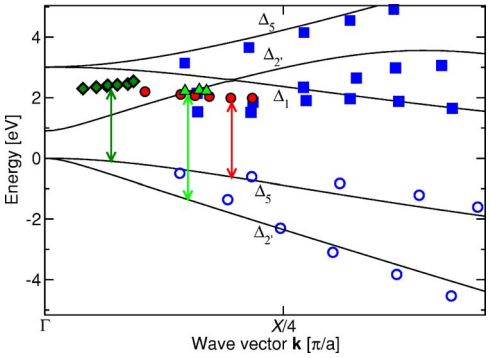

FIG. 11. (Color online) Mapping the experimental Raman data onto the electronic band structure. Squares and open circles (blue) denote experimental data obtained by angle-resolved photoemission spectroscopy and inverse photoemission spectroscopy, respectively (Refs. 38 and 39). Solid lines are our calculations of the electronic band structure. The diamonds were obtained from measurements on the (100) surface with an underlying "across Γ" process and the symmetry-allowed Δ_1 acoustic phonon. For the corresponding VB the band with symmetry Δ_5 was taken. The solid circles and triangles were obtained from the shift of the peaks measured on the (110) surface with a underlying $\Delta\Delta_l$ process and the allowed Σ_1 optical phonon. For the squares and circles we take the $\Delta_{2'}$ and Δ_5 bands as the VB, respectively, in accordance with our considerations in Sec. III B 1. Arrows indicate the optical transitions. We use the same symbols as in Fig. 1(b). Note that a data point (blue square) is hidden under the solid triangles.

V. CONCLUSION

In summary, we presented a comprehensive study of the energy-dependent Raman modes of germanium. Our interpretation in terms of double resonance can explain the observations in both the acoustic and optical ranges. We showed that the process "$\perp E_1$" proposed up to now is not sufficient to explain the observations. We proposed therefore different scattering processes and transitions in different regions of the Brillouin zone. We elaborated the surface-driven k-selective mechanism proposed in Ref. 8 to explain the polarization dependence of the observed shifts, which otherwise cannot be expected in a cubic system. Using the suggested processes we performed a mapping of the experimental data onto the calculated phonon dispersion and obtained excellent agreement. A method that allows a simultaneous quantitative discussion of double-resonant processes for the acoustic and optic phonons and electronic bands of a solid was presented.

*Electronic address: marcel@physik.tu-berlin.de

[1] G. Pérez, A. Bernal-Oliva, E. Márquez, J. González-Leal, C. Morant, I. Génova, J. Trigo, and J. Sanz, Thin Solid Films **485**, 274 (2005).
[2] Z. Sun, S. Wei, A. V. Kolobov, H. Oyanagi, and K. Brunner, Phys. Rev. B **71**, 245334 (2005).
[3] J. H. Parker, Jr., D. W. Feldman, and M. Ashkin, Phys. Rev. **155**, 712 (1967).
[4] B. A. Weinstein and M. Cardona, Phys. Rev. B **7**, 2545 (1973).
[5] M. A. Renucci, J. B. Renucci, R. Zeyher, and M. Cardona, Phys. Rev. B **10**, 4309 (1974).
[6] V. Gaisler, N. I. G. M. Singukov, and A. Talochkin, JETP Lett. **45**, 441 (1987).
[7] W. Cheng, S. F. Ren, and P. Y. Yu, Phys. Rev. B **68**, 193309 (2003).
[8] D. J. Mowbray, H. Fuchs, D. W. Niles, M. Cardona, C. Thomsen, and B. Friedl, in *Proceedings of the 20th ICPS*, edited by E. M. Anastassakis and J. D. Joannopoulos (World Scientific, Singapore, 1990), p. 2017.
[9] M. L. Bansal, A. K. Sood, and M. Cardona, Solid State Commun. **78**, 579 (1991).
[10] C. Thomsen and S. Reich, Phys. Rev. Lett. **85**, 5214 (2000).
[11] J. Maultzsch, S. Reich, and C. Thomsen, Phys. Rev. B **64**, 121407(R) (2001).
[12] S. Reich, C. Thomsen, and J. Maultzsch, *Carbon Nanotubes, Basic Concepts and Physical Properties* (Wiley-VCH, Berlin, 2004).
[13] Z. V. Popovic, M. Cardona, E. Richter, D. Strauch, L. Tapfer, and

K. Ploog, Phys. Rev. B **43**, 4925 (1991).
[14] C. Thomsen and S. Reich, in *Light Scattering in Solids IX*, edited by M. Cardona and R. Merlin, Topics in Applied Physics (Springer, Heidelberg, 2005).
[15] M. Cardona, in *Light Scattering in Solids II*, edited by M. Cardona and G. Güntherodt, Topics in Applied Physics Vol. 50 (Springer, Berlin, 1982), p. 19.
[16] R. M. Martin and L. M. Falicov, in *Light Scattering in Solids I: Introductory Concepts*, edited by M. Cardona, Topics of Applied Physics Vol. 8 (Springer-Verlag, Berlin, 1983), p. 79.
[17] J. Maultzsch, S. Reich, and C. Thomsen, Phys. Rev. B **70**, 155403 (2004).
[18] P. Ordejón, E. Artacho, and J. M. Soler, Phys. Rev. B **53**, R10441 (1996).
[19] J. M. Soler, E. Artacho, J. D. Gale, A. García, J. Junquera, P. Ordejón, and D. Sánchez-Portal, J. Phys.: Condens. Matter **14**, 2745 (2002).
[20] J. P. Perdew and A. Zunger, Phys. Rev. B **23**, 5048 (1981).
[21] N. Troullier and J. L. Martins, Phys. Rev. B **43**, 1993 (1991).
[22] H. J. Monkhorst and J. D. Pack, Phys. Rev. B **13**, 5188 (1976).
[23] M. Cardona, Solid State Commun. **133**, 3 (2005).
[24] N. Bernstein, M. J. Mehl, and D. A. Papaconstantopoulos, Phys. Rev. B **66**, 075212 (2002).
[25] S. Richard, F. Aniel, and G. Fishman, Phys. Rev. B **70**, 235204 (2004).
[26] K. Kunc and R. M. Martin, Phys. Rev. Lett. **48**, 406 (1982).
[27] G. Nilsson and G. Nelin, Phys. Rev. B **3**, 364 (1971).
[28] T. Inui, Y. Tanabe, and Y. Onodera, *Group Theory and its Applications in Physics* (Springer-Verlag, Berlin, 1990).
[29] E. Anastassakis and E. Burstein, J. Phys. Chem. Solids **32**, 313 (1971).
[30] S. Reich and C. Thomsen, Philos. Trans. R. Soc. London, Ser. A **362**, 2271 (2004).
[31] M. Lax, in *Proceedings of the 6th ICPS*, edited by A. C. Stickland (The Institute of Physics and the Physical Society, London, 1962), p. 395.
[32] M. Lax and J. J. Hopfield, Phys. Rev. **124**, 115 (1961).
[33] J. L. Birman, Phys. Rev. **127**, 1093 (1962).
[34] J. M. Zhang, M. Giehler, A. Gobel, T. Ruf, M. Cardona, E. E. Haller, and K. Itoh, Phys. Rev. B **57**, 1348 (1998).
[35] D. Olego and M. Cardona, Solid State Commun. **39**, 1071 (1981).
[36] R. Saito, A. Jorio, A. G. Souza Filho, G. Dresselhaus, M. S. Dresselhaus, and M. A. Pimenta, Phys. Rev. Lett. **88**, 027401 (2002).
[37] J. Maultzsch, S. Reich, U. Schlecht, and C. Thomsen, Phys. Rev. Lett. **91**, 087402 (2003).
[38] X. H. Chen, W. Ranke, and E. Schroder-Bergen, Phys. Rev. B **42**, 7429 (1990).
[39] J. E. Ortega and F. J. Himpsel, Phys. Rev. B **47**, 2130 (1993).